Understanding the Effect of Confinement on the Liquid–Gas Transition: A Study of Adsorption Isotherms in a Family of Metal–Organic Frameworks

Marta de Toni, Pluton Pullumbi, François-Xavier Coudert, Alain H. Fuchs

Understanding the Effect of Confinement on the Liquid-Gas Transition: A Study of Adsorption Isotherms in a Family of Metal–Organic Frameworks

*Marta De Toni,[a,b] Pluton Pullumbi[b], François-Xavier Coudert,[a] and Alain H. Fuchs[a,]**

a. CNRS & Chimie ParisTech, 11 rue Pierre et Marie Curie, F-75005 Paris, France

b. Air Liquide, Centre de Recherche Claude Delorme, Jouy-en-Josas, France

AUTHOR EMAIL ADDRESS: alain.fuchs@cnrs-dir.fr

ABSTRACT:

We present here a molecular simulation study of the adsorption of CO_2 in a family of IRMOF metal–organic frameworks with varying pore size and chemical nature, as controlled by the linker length and the strength of the MOF–CO_2 interactions. This extension of previous theoretical and experimental characterizations (Walton et al., *J. Am. Chem. Soc.* **2008**, *130*, 406–407) provides a coherent explanation and a generic framework to understand the presence or absence of step in the sorption isotherms, in terms of the effect of confinement on the liquid–gas phase diagram of the adsorbate. This branch of the phase diagram is calculated explicitly for CO2 @ IRMOFs, and compared to previous work on families of zeolites and other metal–organic frameworks.

KEYWORDS: adsorption; metal–organic frameworks; carbon dioxide; confinement; phase diagram; molecular simulation.

Introduction

When a molecular fluid is confined by solid substrates to spaces of nanoscopic dimensions, the effect of confinement is to add a new relevant length scale to the physics of the system, namely the separation of the solid surfaces, i.e. the pore size. As a consequence, the properties of the confined fluid are altered from those of the bulk fluid in the same thermodynamic conditions, usually controlled by the temperature T and the chemical potential μ.[1] Moreover, while simple confining geometries such as nonconnected slit pores or cylindrical pores can be defined by a single quantity (respectively, the pore width and the pore diameter), the geometry of the confining matrix in many real-life systems cannot be described by a unique scalar quantity. In nanoporous solids, for example, the description of the confinement needs to account for local geometry (shape and size heterogeneity of the various pores), topology (how are they connected to each other?) and regularity (is the system crystalline or disordered, and if so, what is the distribution of pore sizes?). Finally, in addition to these effects of confinement, the mere proximity of the fluid to the surface of the solid induces modification of the behavior of the fluid, a surface effect due to the presence of the fluid–solid interface. The interactions of the fluid with the surface can be characterized by their strength, that is the absolute value of the fluid–wall interaction, but in many real-life systems one also has to take into account the intrinsic heterogeneity of the pore surface. While ideal (defect-free) carbon nanotubes[2,3] and all-silica zeolites[4,5] can be considered to have a homogeneous inner surface, most substrates are far from being free of defects (experimental carbon nanotube samples[6] or zeolites[7]), and many materials present an intrinsic heterogeneity: cationic zeolites, hybrid organic–inorganic materials and biological channels are rather self-explanatory examples of heterogeneous inner surfaces.

All these features, which render confined fluids fascinating both from an experimental and from a theoretical point of view, have lead to numerous studies concerned either with various fluids, from simple atomic and molecular gases and liquids, to more complex systems such as flexible alkanes, and diverse confining matrices described in the adsorption literature with different levels of structural details

going from model systems[8] such as homogeneous slit,[9] cylindrical[10] and spherical cavities,[11] all the way to realistic atomistic representation of industrially-relevant heterogeneous catalysts such as chemically complex cationic zeolites[12] and hydrophobic pockets in proteins.[13,14] With the large number of adsorption studies published by the community, both ends of the gamut of systems are pretty well covered. On one hand, the effect of confinement due to homogeneous materials with simple geometries has been rather well studied, both by analytical statistical mechanics and numerical means, allowing generic conclusions on confinement effects in these systems to be drawn. On the other hand, the theoretical and experimental tools for the study of adsorption in complex (and heterogeneous) chemical environments has made tremendous progress in the last decade, towards understanding the adsorption properties and the behavior of confined fluids in these systems. We believe, however, that there is still work to be done in order to bridge the two ends of this spectrum, by trying to bring some rationalization, and a more generic understanding, of the confinement effects in chemically heterogeneous nanopores.

Previous work in our group has focused on linking these two different kinds of pictures of the confinement effect, by studying the adsorption properties of small molecules (e.g. water) in entire families of materials in a wide range of thermodynamic conditions, varying either the characteristics of the pore (shape, size, connectivity) or the chemical nature of the inner pore surface. This has lead us to study, for example, the effect of the presence of hydrophilic defects in hydrophobic zeolites,[15,16] or the influence of pore size in the calorimetry of water intrusion in all-silica zeolites.[17,18] In this article, we present a molecular simulation study of the adsorption of CO_2 in a family of metal–organic frameworks with varying pore size and chemical nature. We then show how the features of CO_2 adsorption in these materials, such as the presence or absence of step in the isotherm, or the adsorption enthalpies, can be rationalized in a very generic way in terms of the effect of confinement on the liquid–gas phase diagram of the adsorbate. In this particular, we were able to compute explicitly the liquid–gas branch of the phase diagram of confined CO_2, depending on the confining material. We compare these results to previous work on other families of materials (zeolites and metal–organic frameworks) to make the case

that such phase diagrams of confined fluids are a very useful and generic representation of the adsorption properties of nanoporous materials.

Systems

Metal–organic frameworks (MOFs), or nanoporous polymer coordination networks, are a new class of very topical nanoporous crystalline solids, built from metal centers interconnected by organic linkers. These materials display a large range of crystal structures and host–guest properties, due to a combination of tunable porosity, by choice of metal centers and linker length, and functionalization of the internal surface of the material. Among the proposed applications of MOFs, adsorptive storage and separation of strategic gases (H_2, CO_2, CH_4, etc.) are of particular importance and have gained a lot of attention in recent years.[19,20] One of the particularities of MOFs is that whole families of materials that share the same pore geometry and topology can be created, but with different pore sizes. Such families, called *isoreticular MOFs* (IRMOFs), are created by replacing the organic linker in a base material with longer variants display the same ends.[21,22] As a consequence, the linker length and unit cell size grow, while the coordination chemistry, and thus the framework topology, are unchanged.

In this article, we report a molecular simulation study of the adsorption of CO_2 in three MOFs of the IRMOF family: IRMOF-1, -10 and -16. These materials, discovered by Yaghi and coworkers,[21,22] feature oxide-centered Zn_4O tetrahedral clusters as metal centers, connected by dicarboxylate linkers and forming a 3D-connected cubic framework. IRMOF-1, also known as MOF-5, was the first known member of this family, and is an archetypal metal–organic framework, widely studied and now commercially available. Its organic linker is 1,4-benzenedicarboxylate (1,4-BDC) and it has a pore size of ~ 9 Å. Other members of this rich family feature different linkers, both smaller and larger in size, some with functional groups and heteroatoms. The linkers of IRMOF-10 and IRMOF-16 are chemically similar to 1,4-BDC, except that they contain 2 and 3 benzene rings, respectively, between their two carboxylate extremities. Their pore sizes are larger than IRMOF-1, at 13 Å and 16 Å; the pore volumes

and specific area also increase with linker length. The linkers and graphical representations of the unit cell of these three materials are displayed in Figure 1.

Simulation Methods

The adsorption isotherms were calculated at different temperatures in a wide range of pressure by grand canonical Monte Carlo (GCMC) simulations. Each point of each isotherm is obtained by a single GCMC run, calculating the average number of adsorbed molecules per unit cell of the material for given thermodynamic parameters: chemical potential μ and temperature T. Each GCMC simulation was run for at least 30 million steps. Pre-insertion,[23] orientation[24,25] and displacement bias moves were used to accelerate the convergence. The chemical potential of CO_2 was related to pressure by considering the gas in the external (fictitious) reservoir as ideal. The pressures considered in the study are low enough to make this approximation, which amounts to equating the pressure and fugacity of the bulk CO_2 phase. The thermodynamic properties of bulk CO_2 in the model considered, on the contrary, were calculated with Gibbs ensemble Monte Carlo (GEMC).[26] This allows the simulation of the liquid–gas equilibrium without considering an explicit interface, and thus without including the surface tension effects that are negligible in the thermodynamic limit. To estimate the location of the critical point from GEMC simulation at $T < T_c$, we used the classical rectilinear diameter rule:

$$\frac{\rho_L + \rho_G}{2} = \rho_c + C \times \left(T_c - T\right) \quad (1)$$

and the following scaling relationship for the width of the coexistence curve:[27]

$$\rho_L - \rho_G \propto \left(T_c - T\right)^{\beta} \quad (2)$$

The fitted value of critical exponent β, 0.295, is close to the expected value of 0.325. The details of the GEMC simulations and fits are given in Figure 3S.

Both the sorbate and the adsorbents are considered as rigid frameworks, represented by atomistic models. CO_2 molecules are described by the TraPPE model,[28] which contains three Lennard-Jones centers and three partial charges born by the atoms: a negative charge of –0.35 e is placed on each

oxygen, and a positive charge of +0.7 *e* on the carbon. The IRMOF materials were described with the inclusion of only the repulsion–dispersion energy, modeled by Lennard-Jones 6–12 potentials. The Lennard-Jones parameters for the atoms of the material were taken from the DREIDING force fied,[29] and the Lorentz-Berthelot mixing rules were used to describe the IRMOF–CO_2 interactions. No electrostatic interaction is taken into account between the IRMOF and CO_2. This model and this choice of parameters were shown in a previous work by Walton et al. on the same systems to yield good agreement with the experimental isotherms for IRMOF-1 on a wide range of temperature.[30] In order to improve the efficiency of the calculations, the repulsion–dispersion interaction energies with the sorbate were precomputed on a cubic grid (with a mesh size of approximately 0.2 Å) and stored on disk for later use during the simulations, during which the energy at any point in space was interpolated from the values on the nearest grid points.

Results and Discussion

Influence of pore size

We start this discussion by studying the effect of pore size on the adsorption of CO_2 in the IRMOF family. Figure 2 presents the equilibrium adsorption isotherms in IRMOF-1, IRMOF-10 and IRMOF-16 for various temperatures in the range 195–300 K, using a logarithmic pressure scale. These results are in excellent agreement with the previously reported isotherms of Walton *et al*.[30] Each point in these isotherms corresponds to the thermodynamic equilibrium, and dashed lines represent first-order phase transitions (we explain in detail in the next section how equilibrium and transitions were characterized). Figure S1 (in the supplementary information) also displays the isotherms in linear pressure scale. It can be clearly seen that, for all three materials in this temperature range, the isotherms are stepped, presenting an S shape in linear scale. This shape of isotherm is classified by IUPAC as type V isotherms.[31] When it is encountered in microporous materials, it is a sign that the affinity of the fluid for the material is weak; on the contrary, if fluid–solid affinity is high, adsorption will typically follow a type I, Langmuir-like isotherm. This phenomenon is most often observed with highly polar molecules,

and has been studied in depth for water adsorption on hydrophobic, hydrophilic or heterogeneous materials, both for microporous and mesoporous solids. It finds its roots in the relative values of the fluid–fluid and fluid–solid interactions, which explains why it is predominantly observed in highly polar materials, even though it is a very generic phenomenon arising from the fluid's phase diagram (as we will show later) and can be observed for any fluid in a suitably chosen range of temperature.

It the case of CO_2 in IRMOFs, the isotherms show that the materials are only weakly attractive to CO_2 in the temperature range explored. The isotherms furthermore show quite clearly in all cases that, at low temperature, the adsorption follows a first-order transition, with a discontinuity of the isotherm, while at higher temperature it is a continuous process. This is evidently similar to the liquid–gas equilibrium of bulk fluids, which present a critical temperature (T_c), below which a liquid–gas phase transition is observed upon compression and above which the fluid is supercritical. Indeed, the series of adsorption isotherms in fig. 2, if plotted with their axes interchanged (as pressure vs. density isotherms, displayed in Figure 2S), correspond to compression curves for the adsorbed phase, with the liquid–gas coexistence area (colored in yellow in Fig. 2S). From there, if one calculates enough adsorption isotherms for various temperatures, it is possible to localize the critical point of CO_2 adsorbed in each IRMOF material, and construct explicitly the full liquid–gas branch of the phase diagram of the confined fluid.

This phase diagram for CO_2 confined in IRMOF-1, -10 and -16, is presented in Figure 3. The liquid–vapor equilibrium of bulk CO_2 is also plotted on this, as obtained from Gibbs ensemble Monte Carlo simulations using the same model for CO_2 as in the GCMC simulations. Solid lines correspond to liquid–gas equilibrium, the singular points ending these lines are the critical points for each system, and the dotted lines correspond to the position of the continuous adsorption transition in the supercritical region (as determined by the inflexion of the isotherm).

Turning to the effects of confinement on the phase diagram of CO_2, the first thing to be noted is that the critical temperature is lowered by the presence of the IRMOF material. Moreover, the smaller the confinement scale, the smaller the critical temperature is. This effect is consistent with what we systematically observed in previous work on different materials (various zeolites and MOFs). It can be

linked to the theoretical studies of the phase diagram of fluids confined in slit and cylindrical pores, which show a similar evolution. In dimensions strictly greater than one, including the case of our three-dimensional system here, there is a true critical point for the liquid-vapor transition, which belongs to the universality class of the 3D Ising model. For a bulk system, this critical point occurs when the correlation length of the system diverges; in the case of fluid inside a host matrix, it occurs when the correlation length reaches the pore dimension.[32] This happens before it point of divergence, which corresponds to the bulk critical point. Moreover, the smaller the pore size is, the further the confined critical point will be from the bulk, and the smaller the critical temperature will be.

The second feature worth noting on Fig. 3 is that, for a given temperature below the critical point, the liquid–gas equilibrium pressure decreases with the confinement. To rationalize this effect in terms of macroscopic, physicochemical properties of the fluid and the materials, we use here the Laplace-Washburn equation. While it does not apply to such small scales, it does however capture the trends observed pretty well, even at small pore sizes, as was shown by Coasne et al. in work on porous silicas.[33] The Laplace-Washburn equation[34] describes the adsorption pressure P in pores of radius r_p as follows:

$$P = -\frac{2\gamma_{LV}\cos\theta}{r_p} \tag{3}$$

where γ_{LV} is the fluid–wall interfacial tension and θ the contact angle. In the case of CO_2 in IRMOFs, P decreases with r_p, meaning that $\cos\theta > 0$. This shows that the CO_2 wets the internal surface of the IRMOF nanopores, if we can consider them to be similar enough that the variation in $\cos\theta$ between members of the family is smaller than that of $1/r_p$.

Finally, a third point of interest in this phase diagram of confined CO_2 is that both the first-order phase transition boundary (the solid lines) and the adsorption transition in the supercritical region (dotted lines) are pretty regular. In fact, when plotted as $\log(P)$ vs. $1/T$, they are very close to straight lines in this temperature range. Linking this to the Clausius-Clapeyron equation, commonly used for estimating differentials in the isosteric heat of adsorption from pressure and temperature data measured at the same

adsorption experiment, means that the latent heat of the phase transition is close to constant in this 100 K-wide range of temperature, which potentially allows one to predict phase diagrams such as that of Fig. 3 from a relatively small number of points.

Characterization of thermodynamic equilibrium

We shall say here a few words about how the equilibrium isotherms are calculated, because their determination is an important prerequisite for the calculation of confined fluid's phase diagram. Direct molecular simulations in the Grand Canonical ensemble, near first-order phase transitions, are noticeably hard to converge. Isotherms obtained from GCMC simulations can even present "hysteresis loops", looking similar to the ones observed experimentally, because the number of adsorbed molecules at a given chemical potential may depend on the initial state of the simulation, like whether the run started from an empty or a fully packed simulation box. In the materials reported here, we have no such difficulty as the CO_2–CO_2 interactions are apparently weak enough (i.e. not as strong as the water–water interactions for instance), that no such hysteretic effect is observed. However, even then, the quantities that one can extract from as averages of each molecular simulation run need to be considered with care.

Figure 4 reports the example of CO_2 adsorption in IRMOF-16 at 250 K, which exhibits a first-order transition. The blue symbols correspond to the average number of molecules along each GCMC run, and it can be seen from them that the curve goes smoothly from confined gas (low N_{ads}) to confined liquid (high N_{ads}). However, if one inspects these GCMC runs further, we find that while the evolution of $\langle N_{ads} \rangle$ is continuous, the values taken by N_{ads} along the simulations are distributed according to a bimodal histogram, corresponding to both metastable states. In addition, along the simulation, the system goes back and forth between these two states, with the time spent in each state (and thus the overall average) depending on the chemical potential. These metastable states are indicated as empty black symbols in Fig. 4. Because we are interested here in the behavior of adsorption at thermodynamic equilibrium, we needed to measure the equilibrium transition pressure for each temperature, regardless of the presence of hysteresis. We achieved that by taking as equilibrium pressure (in green on Fig. 4) the

pressure for which both metastable states are equiprobable along the GCMC simulation. This was possible because the free energy barrier for the adsorption process was relatively easily crossed along the simulation, due to the weak CO_2–CO_2 interaction. This is not true for adsorption of more polar fluids, where free energy (or density of states) techniques must be used to determine the position of the thermodynamic equilibrium, as we showcased recently with a study on water adsorption in a hydrophobic zeolites and MOF.[35,36]

Influence of sorbate–adsorbent interactions

In order to study the influence of the sorbate–adsorbent interactions on the phase diagram of the confined fluid, it is necessary to be able to modify the chemistry of its internal surface without changing the pore shape, size and topology. Two possible avenues suggested themselves for this: choosing other members of the IRMOF family with a pore size close to IRMOF-1, -10 or -16, but with functionalized linkers; or making nonphysical modifications to the parameters of the molecular simulation, increasing artificially the CO_2–IRMOF interactions. The first alternative is difficult to implement: functionalizing the benzene rings by adding side linkers modifies the pore geometry and volume in a way that interferes with our goal, so that the only practical way to go was to add heteroatoms to the rings, e.g. introducing nitrogen atoms. This, however, adds specific interactions which we want to avoid, and is not controllable in a continuous fashion. Furthermore, such substituted materials are hypothetical, as there are no such known members of the IRMOF family.

Thus, we performed a study of CO_2 adsorption in IRMOF-1 with varying IRMOF–CO_2 interactions. We did that by varying homogeneously the strength of the interaction, scaling it by a factor λ. This multiplicative factor affects the whole adsorbate–solid interactions. As expected, this scaling of the Lennard-Jones ε_{ij} cross-interaction parameters induces a linear scaling of the adsorption enthalpies, ΔH_{ads}, in the limit of low loading (measured by NVT simulations of one probe molecule in the unit cell, and reported in Table 1S for a few values of λ). Figure 5 presents the adsorption isotherms of CO_2 at 208 K, for different values of λ in the range 1–3. The overall effect of increasing λ is clear and expected:

as the sorbate–solid interactions increase, the adsorption transition occurs at lower pressure. Moreover, the slope of the isotherm at low pressure (the Henry constant) increases, as $K_H = K' \exp(-\Delta H_{ads}/RT)$, and the inflexion point of the isotherm moves to lower pressure: it shifts gradually from a type V to a type I isotherm. In this particular example, adsorption follows a type I (Langmuir-like) isotherm for $\lambda \geq 2.7$, where the isotherm does not present an inflexion point any more. Finally, as the walls of the nanoporous become more attractive to the fluid, it is to be noted that the saturation uptake, i.e. the quantity adsorbed on the plateau of the isotherm, increases. This means that the effective pore volume accessible to the material is slightly augmented, a point to which we will return later in the discussion.

Figure 6 presents the confined gas–liquid phase diagram for values of λ between 1 and 1.6. It was constructed similarly to that of regular IRMOF-1, from swarms of isotherms at various temperatures for each value of λ. As was observed on fig. 5, it shows that adsorption pressure decreases with increasing adsorption enthalpy, both in the first-order transition and the supercritical regions. What is less expected, however, is the nonmonotonic behavior of the critical temperature, which goes up from $\lambda = 1$ to $\lambda = 1.2$, and then down from $\lambda = 1.2$ to $\lambda = 1.6$. We attribute this to the competition of two different effects: the increase of CO_2 adsorption enthalpy, and the increase of the accessible pore volume for the fluid. For the two points at $\lambda = 1.5$ and $\lambda = 1.6$, which have very similar saturation uptake, the effect is solely that of CO_2–MOF interactions: stronger interactions solid–sorbate interactions lower the critical point. This in agreement with the fact that, at a fixed temperature, increasing λ moves the adsorption towards smoother isotherms (i.e. supercritical behavior) and, in the end, a transition from type V to type I behavior (far above the supercritical point). To this trend adds the effect of accessible volume change: as noted from the saturation uptake of the isotherms, increasing sorbate–MOF interactions increases the accessible pore volume, and thus shifts the critical point to higher temperatures. The resulting trend is the nonmonotonic variation observed in Fig. 6.

Comparison to other systems

The {CO_2, IRMOF} couple studied herein is the first system for which we have explicitly calculated the confined fluid phase diagram along a family of materials. We have, however, previously studied water adsorption in various series of materials: hydrophobic MOFs with various degrees of $–CH_3$ functionalization;[36] all-silica zeolites of various pore sizes and connectivities;[15,16] series of hydrophilic zeolites with varying concentration (and spatial distribution) of hydrophilic "silanol nest" defects.[17,18] The confined fluid phase diagrams obtained from the experimental and molecular simulation adsorption data in these families of materials are reported in Figure 7. This highlights how, using the liquid–gas phase diagram of the confined fluid as a representation of the adsorption properties of the material, one can rationalize and even predict their evolution for a whole family of materials. We have already discussed above the effects of pore size and guest–solid interactions, based on the case of CO_2 in IRMOFs. We now can interpret the other phase diagrams in light of this knowledge.

For H_2O in Al(OH)(ndc) (upper-right quadrant), we see that functionalization of the internal surface of the pore reduces both the pore size and the H_2O–Al(OH)(ndc) interactions, as methyl groups border the pore instead of the more dispersive naphthalene rings. As a consequence, the critical temperature decreases and increases the adsorption pressure upon functionalization. All materials are wetting, though, as the adsorption pressure (P_{ads}) is in all cases smaller than water saturation pressure (P_{sat}). In the case of all-silica zeolites (lower-left quadrant), the situation is even simpler: the pore surface chemistry is unchanged (SiO_2, bordered with oxygen atoms while the silicon atoms are deeper inside the walls). Such materials are strongly nonwetting when ideal (i.e. free of structural defects and templating molecules), and consistently with the Laplace-Washburn equation, the adsorption pressure increases with confinement. This explains why, at room temperature, water intrusion in small-pore all-silica zeolites exhibits all the signs of a smooth, continuous transition, while for higher pore sizes it displays first-order transitions.

Finally, the lower-right quadrant of Fig. 7 shows a tentative confined phase diagram for water adsorption in hydrophobic zeolites with varying concentration of hydrophilic defects. This diagram was drawn from previous works on these systems. While the defect-free zeolite is nonwetting, i.e. its

adsorption pressure is higher than water saturation pressure, the introduction of silanol groups in the zeolitic framework increases the water–solid interactions drastically. As a consequence, the adsorption happens at lower pressure, eventually crossing the bulk equilibrium line, i.e. going from nonwetting to wetting. The critical temperature is lowered by the presence of these defects, as is evidenced by the observed change in isotherm shape, which become smoother and without hysteresis. At very high defect concentration, one would observe a simple type I isotherm, as is observed for cationic zeolites.

As a conclusion of this quick comparison, we see that the liquid–gas phase diagram of the confined fluid is a useful generic tool for rationalizing the adsorption behavior in families of related materials. It allows to characterize (and predict) the adsorption properties of the materials in a wide range of temperature and pressure, when the host solid's characteristics are modified. This approach could be further generalized by introducing some descriptors that would be useful for building correlations for screening nanoporous materials for a particular application. Such descriptors could be for example the ratio of solid–fluid to fluid–fluid interactions, some non-dimensional numbers characterizing the energetic heterogeneity of the accessible surface and accessible volume of the porous matrix.

Conclusions

We presented a molecular simulation study of the adsorption of CO_2 in a family of IRMOF metal–organic frameworks with varying pore size and chemical nature, as controlled by the linker length and strength of the MOF–CO_2 interactions. We showed how the features of CO_2 adsorption in these materials, such as the presence or absence of step in the isotherm, or the adsorption enthalpies, can be rationalized in a very generic way in terms of the effect of confinement on the liquid–gas phase diagram of the adsorbate. In this particular, we were able to compute explicitly the liquid–gas branch of the phase diagram of confined CO_2, depending on the confining material. We compared these results to previous work on other families of materials (zeolites and metal–organic frameworks) to make the case that such phase diagrams of confined fluids are a very useful and generic representation of the adsorption properties of nanoporous materials, yielding much information of practical consequences,

such as: “what thermodynamic conditions they perform best?” or: “what pore radius modification or pore surface functionalization would improve them in a given set of conditions?”

Acknowledgment. This work was supported by the Agence Nationale de la Recherche Technologique, and by the Agence Nationale de la Recherche, under contracts ANR-06-CO2-007 and BLANC06-3_144027. The authors thank Anne Boutin, Randy Snurr and Tina Düren for fruitful discussions.

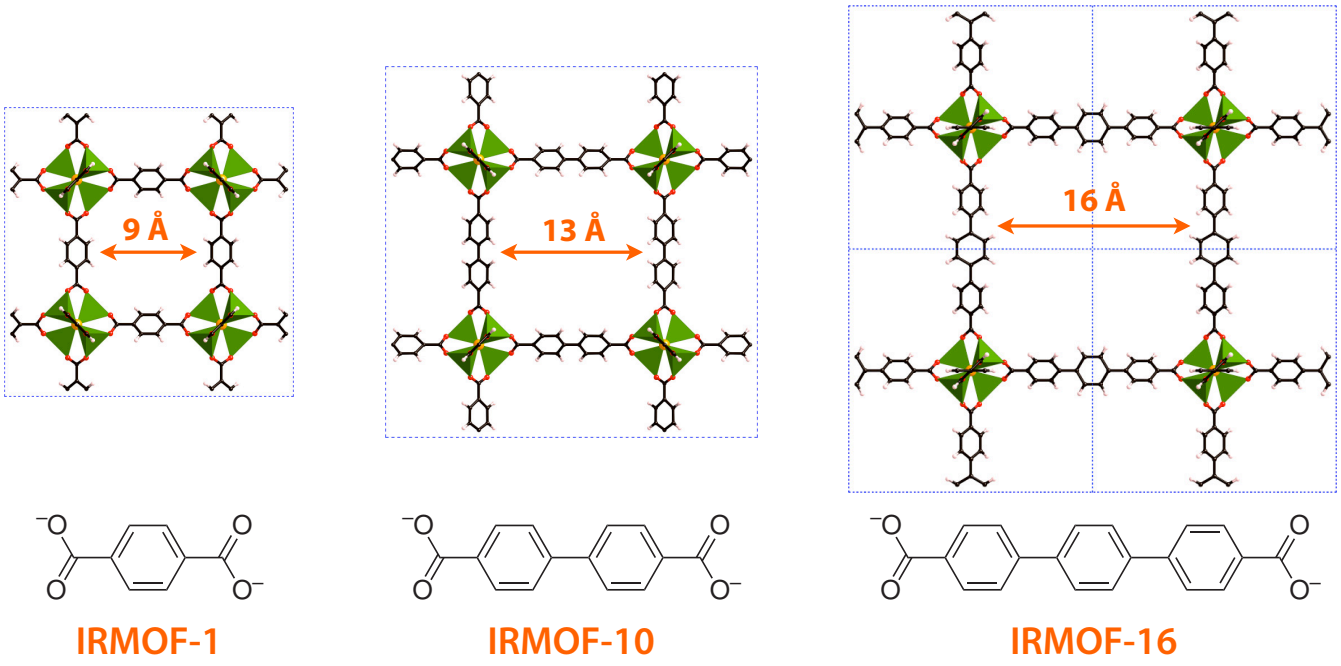

Figure 1. Representation of the IRMOFs studied in the present work: IRMOF-1, IRMOF-10 and IRMOF-16: unit cells, pore size and linker. For IRMOF-16, a 2×2×2 supercell is depicted.

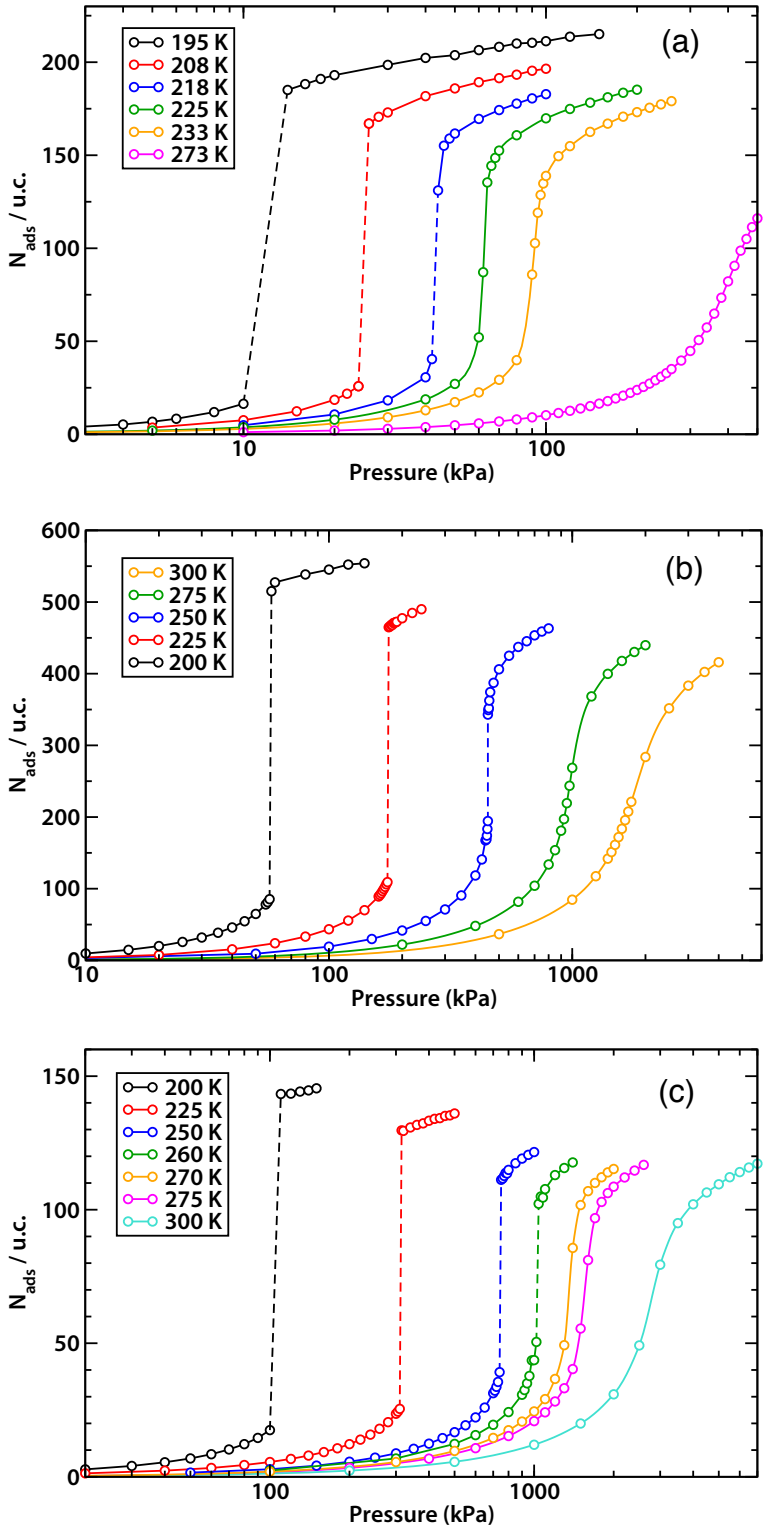

Figure 2. CO_2 adsorption isotherms in IRMOF-1 (a), IRMOF-10 (b) and IRMOF-16 (c) in the 195–300 K range of temperature. Each symbol corresponds to a single (μ,V,T) GCMC simulation. Lines are added to guide the eye. Vertical dashed lines correspond to first-order phase transitions.

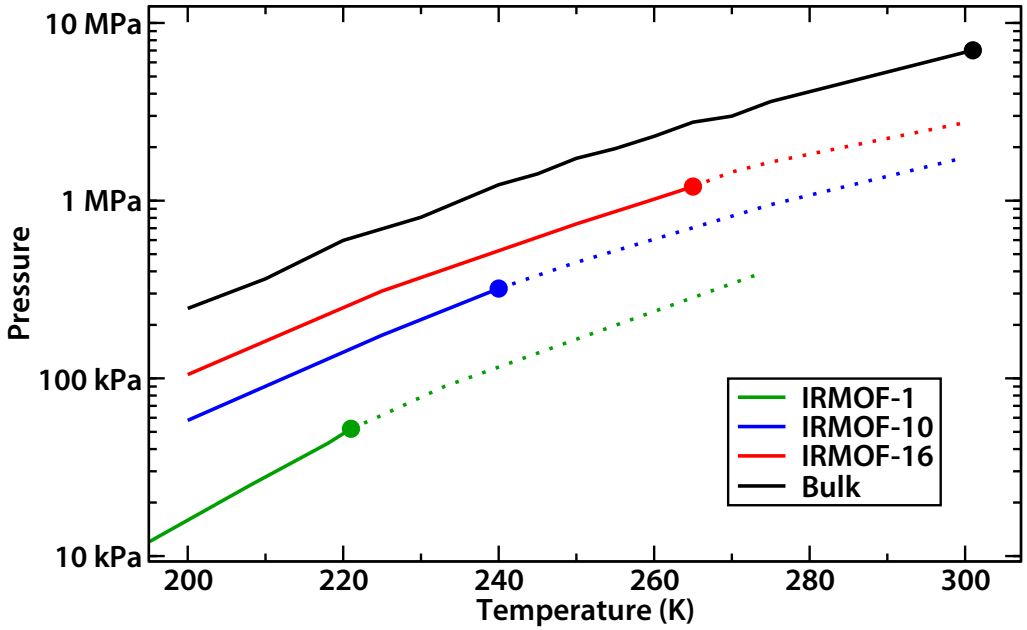

Figure 3. Pressure–temperature phase diagram for CO_2 confined in IRMOF-1, -10 and -16, compared to the bulk phase. Solid lines represent liquid-vapor first-order phase transitions, filled circles indicate critical points and dotted lines indicate continuous adsorption transitions.

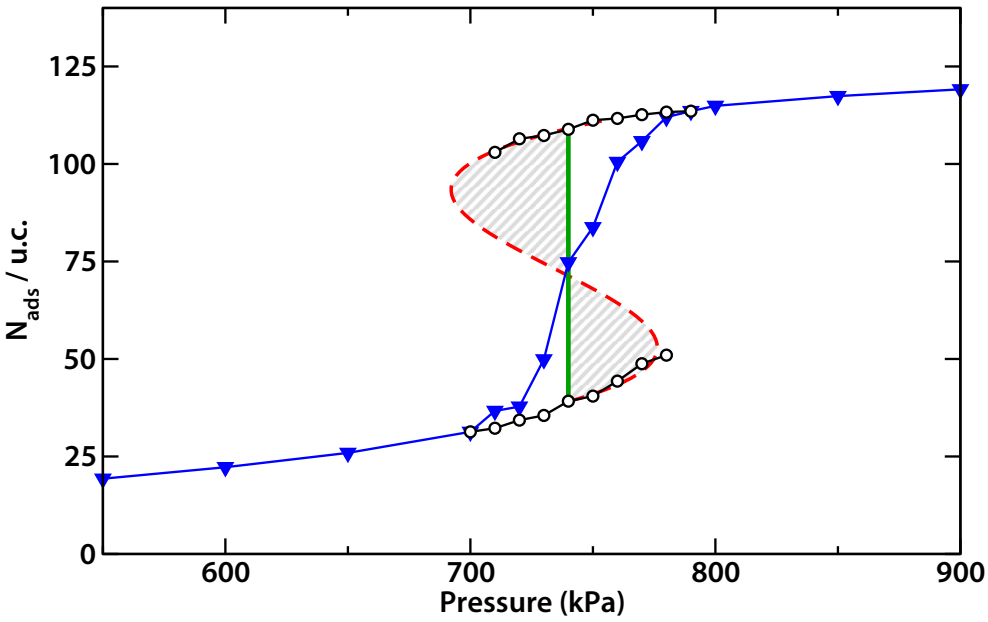

Figure 4. First-order phase transition of CO_2 adsorption in IRMOF-16 at 250 K. Blue triangles correspond to averages from GCMC simulations. Open circles represent individual "empty" and "filled" phases observed in the GCMC simulations in the 700–800 kPa range. The thermodynamic equilibrium pressure is indicated by the vertical green line, and the spinodal (calculated as a third-power best fit complying with Maxwell's rule) is indicated in dashed red.

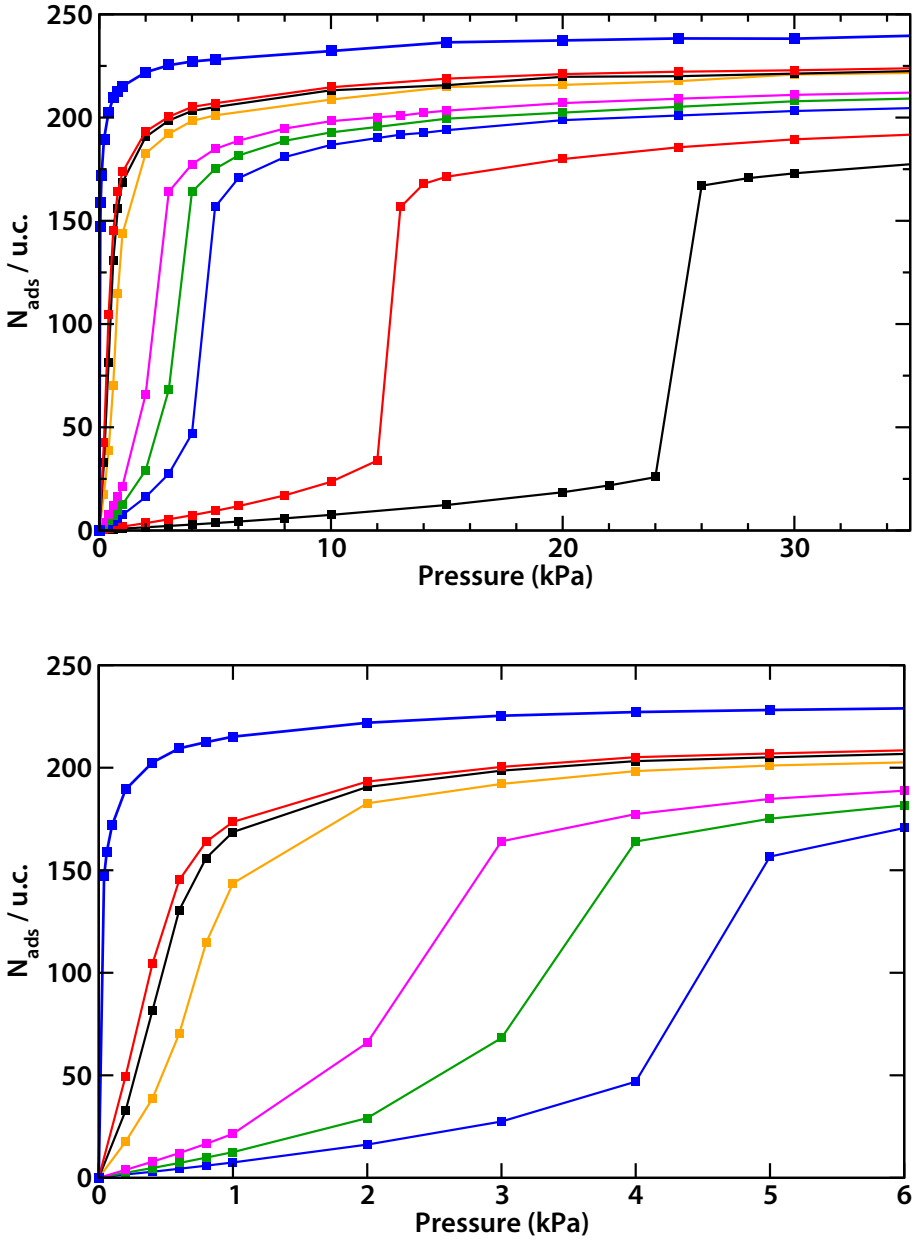

Figure 5. CO_2 adsorption isotherms in IRMOF-1 at 208 K with scaled CO2–IRMOF interactions, for different values of the scaling parameter λ: 1 (black), 1.2 (red), 1.5 (blue), 1.6 (green), 1.7 (pink), 2.0 (orange), 2.5 (black), 2.7 (red) and 3.0 (blue). Lower panel displays a zoom of the low-pressure range (up to 6 kPa).

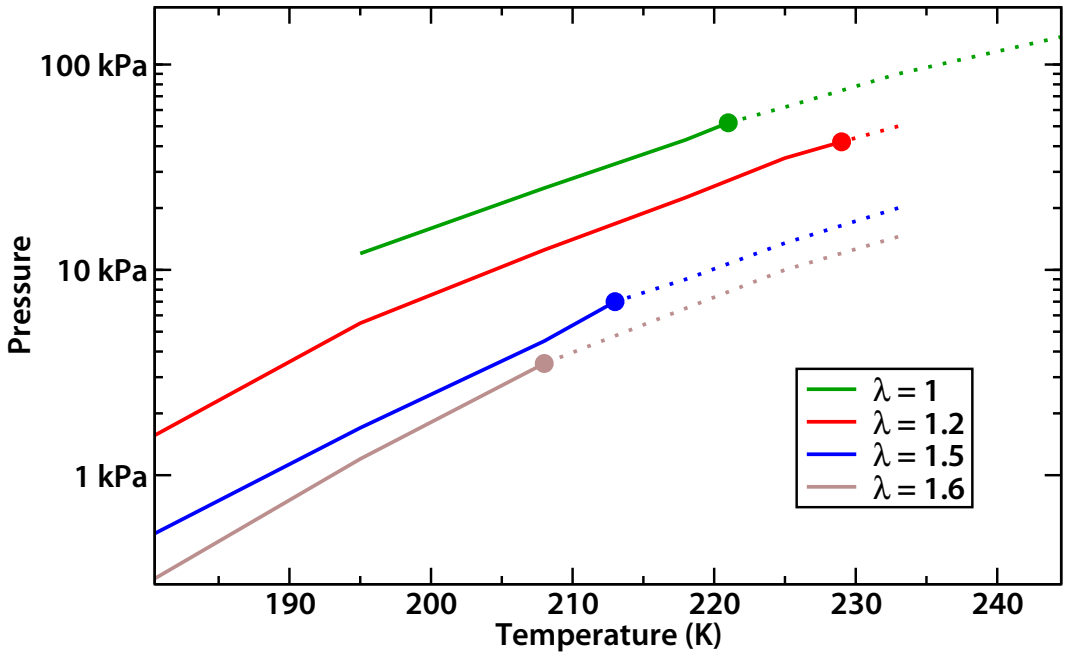

Figure 6. Pressure–temperature phase diagram for CO_2 confined in IRMOF-1, with MOF-CO_2 interactions multiplied by a factor of λ in order to understand the consequences of a modification of the chemical nature of the internal surface of the material, with fixed pore size, geometry and topology.

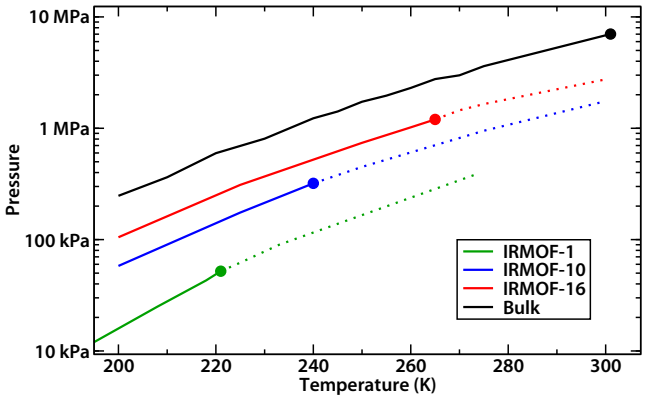

CO_2 in IRMOF-1, -10 and -16 (this work)

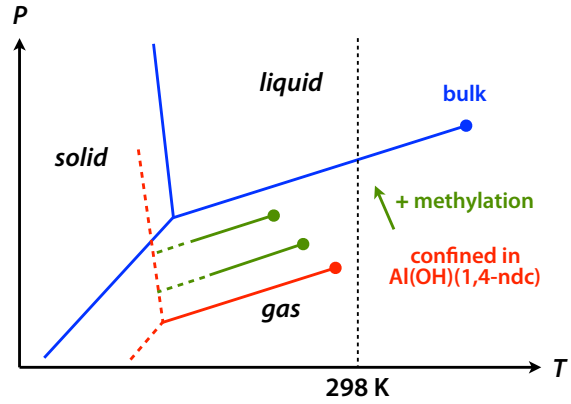

H_2O in Al(OH)(ndc) and
methyl-functionalized derivatives (ref. 36)

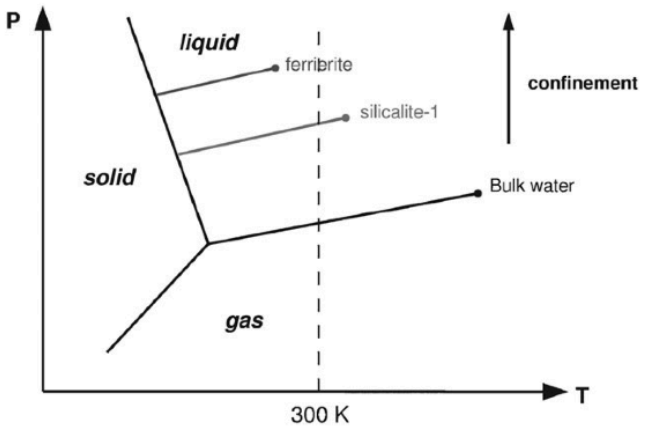

H_2O in all-silica zeolites (ref. 17)

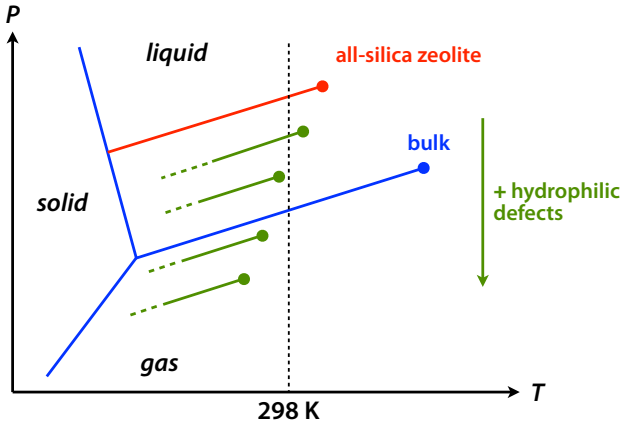

H_2O in a hydrophobic, all-silica zeolites, and upon introduction of increasing concentrations of hydrophilic defects in the zeolite framework (drawn from the results of ref. 16)

Figure 7. Effect of confinement and nature of the internal pore surface for adsorption of polar molecules (CO_2 and H_2O) in various families of nanoporous materials, as evidence by the liquid–gas phase diagram of the confined fluids.

References.

[1] Dietrich, S. *J. Phys.: Condens. Matter* **1998**, *10*, 11469.

[2] Lui, J.-C.; Monson, P. A. *Langmuir* **2005**, *21*, 10219.

[3] Lui, J.-C.; Monson, P. A.; van Swol, F. *J. Phys. Chem. C* **2007**, *111*, 15976.

[4] Caullet, P.; Paillaud, J.-L.; Simon-Masseron, A.; Soulard, M.; Patarin, J. *C. R. Chimie* **2005**, *8*, 245–266.

[5] Blasco, T.; Camblor, M. A.; Corma, A.; Esteve, P.; Guil, J. M.; Martínez, A.; Perdigón-Melón, J. A.; Valencia, S. *J. Phys. Chem. B* **1998**, *102*, 75–88.

[6] Alcaniz-Monge, J.; Linares-Solano, A.; Rand, B. *J. Phys. Chem. B* **2002**, *106*, 3209.

[7] Bolis, V.; Busco, C.; Ugliengo, P. *J. Phys. Chem. B* **2006**, *110*, 4849–14859.

[8] Sarkisov, L.; Monson, P. *Langmuir* **2001**, *17*, 7600–7604.

[9] Kaneko, K.; Cracknell, R. F.; Nicholson, D. *Langmuir*, **1994** *10*, 4606–4609.

[10] Morishige, K.; Nakamura, Y. *Langmuir* **2004**, *20*, 4503–4506.

[11] Ustinov, E. A.; Do, D. D.; Jaroniec, M. *J. Chem. Theory Comput.* **2005**, *1*, 653–661.

[12] Fuchs, A. H.; Cheetham, A. K. *J. Phys. Chem. B* **2001**, *105*, 7375–7383.

[13] Woo, H.-J.; Dinner, A. R.; Roux, B. *J. Chem. Phys.* **2004,** *121*, 6392.

[14] Rasaiah, J. C.; Garde, S.; Hummer, G. *Ann. Rev. Phys. Chem.* **2008**, *59*, 713–740.

[15] Cailliez, F.; Stirnemann, G.; Boutin, A.; Demachy, I.; Fuchs, A. H. *J. Phys. Chem. C* **2008**, *112*, 10435–10445.

[16] Trzpit, M.; Soulard, M.; Patarin, J.; Desbiens, N.; Cailliez, F.; Boutin, A.; Demachy, I.; Fuchs, A. H. *Langmuir*, **2007**, *23*, 10131–10139.

[17] Cailliez, F.; Trzpit, M.; Soulard, M.; Demachy, I.; Boutin, A.; Patarin, J.; Fuchs, A. H. *Phys. Chem. Chem. Phys.* **2008**, *10*, 4817–4826.

[18] Cailliez, F.; Boutin, A.; Demachy, I.; Fuchs, A. H. *Mol. Simulat.* **2009**, *35*, 24–30.

[19] Li, J. R.; Kuppler, R. J.; Zhou, H.-C. *Chem. Soc. Rev.* **2009**, *38*, 1477–1504.

[20] Czaja, A. U.; Trukhan, N.; Mueller, U. *Chem. Soc. Rev.* **2009**, *38*, 1284–1293.

[21] Li, H.; Eddaoudi, M.; O'Keeffe, M.; Yaghi, O. *Nature* **1999**, *402*, 276–279.

[22] Eddaoudi, M.; Kim, J.; Rosi, N.; Vodak, D.; O'Keeffe, M.; Yaghi, O. M. *Science* **2002**, *295*, 469–472.

[23] Mackie, A.; Tavitian, B.; Boutin, A.; Fuchs, A. H. *Mol. Simulat.* **1997**, *19*, 1–10.

[24] Cracknell, R.; Nicholson, D.; Parsonage, N. G.; Evans, H. *Mol. Phys.* **1990**, *71*, 931–943.

[25] Lachet, V.; Boutin, A.; Tavitian, B.; Fuchs, A. H. *J. Phys. Chem. B* **1998**, *102*, 9224–9233.

[26] Ungerer, P.; Tavitian, B.; Boutin, A. *Applications of molecular simulation in the oil and gas industry: Monte Carlo methods*, Editions TECHNIP, 2005.

[27] A. Z. Panagiotopoulos, *Gibbs Ensemble Techniques*, in M. Baus, L.R. Rull and J.P. Ryckaert, "Observation, prediction and simulation of phase transitions in complex fluids", NATO ASI Series C vol. 460, Kluwer Academic Publishers, Dordrecht, The Netherlands (1994), pp. 463-501.

[28] Potoff, J. J.; Siepmann, J. I. *AIChE J.* **2001**, *47*, 1676.

[29] Mayo, S. L.; Olafson, B. D.; Goddard, W. A. *J. Phys. Chem.* **1990**, *94*, 8897.

[30] Walton, K.S.; Millward, A.R.; Dubbeldam, D.; Frost, H.; Low, J.J; Yaghi, O.M; Snurr, R.Q. *J. Am. Chem. Soc.* **2008**, *130*, 406–407.

[31] Sing, K. S. W.; Everett, D. H.; Haul, R. A. W.; Moscou, L.; Pierotti, R. A.; Rouquerol, J. Siemieniewska, T. *Pure Appl. Chem.* **1985**, *57*, 603–619.

[32] Brovchenko, I.; Oleinikova, A. *Interfacial and confined water,* Elsevier, **2008**.

[33] Galarneau, A.; Lefèvre, B.; Cambon, H.; Coasne, B.; Valange, S.; Gabelica, Z.; Bellat, J.-P.; Di Renzo, F. *J. Phys. Chem. C*, **2008**, *112*, 12921–12927.

[34] Washburn, E. W. *Phys. Rev.* **1921**, *17*, 273–283.

[35] Coudert, F.-X.; Cailliez, F.; Vuilleumier, R.; Fuchs, A. H.; Boutin, A. *Faraday Discuss.* **2009**, *141*, 377–398.

[36] Paranthaman, S.; Coudert, F.-X.; Fuchs, A. H. *Phys. Chem. Chem. Phys.* **2010**, *12*, 8123–8129.

Table of Contents Graphic. (3.6 cm × 8.9 cm)